Epitaxial re-solidification of laser-melted Ni-Mn-Ga single crystal

Jakub Toman[a], Darren C. Pagan[b,2], Peter Müllner[c], Markus Chmielus[a]

[a]Department of Mechanical Engineering and Materials Science, University of Pittsburgh, Pittsburgh, PA 15261, USA

[b]Cornell High Energy Synchrotron Source, Ithaca, NY 14853, USA

[c]Micron School of Materials Science and Engineering, Boise State University, Boise, ID 83725, USA

[1]Present address: Materials Science and Engineering Department, The Pennsylvania State University, State College, PA 16802, USA

Abstract

Additive manufacturing (AM) of magnetic shape-memory alloys (MSMAs) allows fuller use of geometry in the design of MSMA parts and avoids the segregation and high cost associated with single crystal production. While most research effort in AM of MSMAs pursues functional foams or polycrystals, epitaxial growth during liquid-phase AM may enable fully-dense single-crystalline MSMA parts, with associated availability of the full blocking stress. We melted a $Ni_{51}Mn_{24.4}Ga_{24.6}$ single crystal with a moving laser spot under several process parameter combinations of laser power and velocity. While tracks created with lower laser travel velocity were almost entirely epitaxial, the track created with highest velocity (10 mm/s) included non-epitaxial columnar grains and grains at the top of the track. Synchrotron-based high-energy diffraction microscopy (HEDM) experiments revealed that mosaic spread of epitaxial material was slightly higher than that of surrounding non-re-solidified material. Our results demonstrate epitaxial growth of Ni-Mn-Ga with minimal grain content using full-melting laser processing.

Introduction

Magnetic shape-memory alloys (MSMA) single crystals, which are primarily targeted for application in actuator devices [1], can undergo repeated strain cycles reaching up to 6, 10 or even 12 % [2,3] at velocities on the orders of 1 or 10 m/s [4] when driven by a magnetic field. However, authors have reported the drawbacks of crystal growth, such as high costs and segregation [5–7], and the geometric capability of AM methods [6–13] as motivation for AM of MSMAs. However, due to the general incompatibility of the magnetic shape memory mechanism with grain boundaries, dense polycrystals may be assumed to produce only insignificant strains [14]. Thus, research groups aim to overcome this barrier by creating high-porosity parts or foams [5,8,9,12,15]. Another possible approach is to induce microstructural texture; however, earlier experiments with highly textured polycrystals have produced at most 1 % strain [16].

Alternatively, epitaxy, the solidification of material with crystal orientation matching that of pre-existing substrate, could be achieved with laser melting of powders upon a pre-existing single crystal, thereby circumventing the limitations of textured polycrystals and the need for porosity. Ullakko et al. suggested to melt powder upon a thin single-crystalline Ni-Mn-Ga plate and performed thermal simulations which indicated that single crystal growth would be possible [17]. Earlier, direct powder deposition with purposeful epitaxy was reported by Gäumann et al., using a single-crystalline Ni superalloy [18,19]. While

equiaxed grains were present in even the most successful cases, the deposits were mostly epitaxial. The authors reported that the number of equiaxed grains can be minimized by a choice of laser power and travel velocity that produces columnar growth, and by mechanical removal at the surface of the final deposition layer. Further work in this direction has resulted in a number of studies with various levels of success [20–25], with examples encompassing powder-bed fusion [26–28] and MCrAlY coatings [29,30]. According to the theory of columnar-to-equiaxed transition described by Gäumann et al., equiaxed growth requires a high ratio between thermal gradient at the solidification interface and growth velocity. The process parameters must create sufficient thermal conditions to avoid equiaxed growth and permit uninterrupted columnar growth at the melt pool boundary, which will continue growth as a single crystal if a single crystal is the source of epitaxy. More broadly, interfacial stability theory states that higher interfacial thermal gradient and lower growth velocity increase stability, with the exception of extremely high velocities [31].

Following the example of Gäumann et al. [19] and others [32,33], our present effort is limited to surface melting without powder deposition, in order to explore process parameters without the added influence of impinging powder particles. Although the magnetic shape memory effect is only possible in the martensite phase, we used room-temperature austenite due to its cubic crystal structure, simplifying analysis of solidification microstructure and diffraction data. The properties of Ni-Mn-Ga martensite processed by laser powder deposition were partially explored in our previous work [34]. Key points of interest in the present study are the incidence of grains, internal misorientation, and the misorientation of re-solidified material relative to the base crystal. We note that in this work, the term “equiaxed grain,” in the sense of a grain nucleated without connection to the substrate [19], is used equivalently to “stray grain”; a stray grain is a grain that is misoriented from the base crystal [20,35]. We also simply use the term “grain” to avoid distinguishing between equiaxed and columnar grains in instances where the shape of the grain is not the focus, but the crystal orientation is.

Methods

A $Ni_{51}Mn_{24.4}Ga_{24.6}$ single crystal was grown with a modified Bridgman-Stockbarger single crystal growth furnace described in [36]. The room temperature structure was $L2_1$-ordered cubic austenite, with a martensitic transformation temperature of $T_M \approx 4$ °C and a Curie temperature of $T_C \approx 97$ °C (see Supplementary Fig. 1). The crystal was cut with a wire saw (Princeton Scientific UNIPRESS WS-22B with SiC abrasive) into two “substrates”, each a prismatic volume of approximately 15 x 3.8 x 2.7 mm. Each substrate was placed on top of a larger Ni plate, with its ~2.7 mm dimension perpendicular to the plate and its as-cut surface facing the laser aperture, and held in place by cyanoacrylate glue at its corners. This assembly was loaded into an Optomec LENS 450 directed laser deposition (DLD) system with a 1070 nm continuous wave Nd:YAG laser and Ar atmosphere with < 0.2 ppm O_2. Each substrate was exposed to the laser spot in a direction parallel to the 3.8 mm dimension at various combinations of nominal laser power *P* and beam travel velocity *V*, creating a total of seven re-solidified tracks (Table 1, Fig. 1. Throughout this article, samples/tracks are referred to short-form as *P*-*V*, e.g. 200-2.5). The laser beam was started sufficiently far from the substrate, and stopped after passing the substrate, to ensure full travel velocity while the laser spot was on the substrate. The laser spot had a calculated diameter of 570 µm, and the power at the spot was measured as 86 W when set to a nominal value of 100 W. Subsequently, samples were cross-sectioned perpendicular to the track (transverse cross-section) by wire saw, mounted,

polished and etched with a mixture of 5 ml H_2O + 5 ml HCl + 1 g $CuSO_4$ by immersion for 5 s (HCl: 36.5–38 w/w %). The presence or lack of a solidified melt pool was identified by optical microscopy (Table 1).

After imaging, samples with non-negligible melting depth were polished again and their mounts dissolved. Surface regions surrounding the melt pool were then prepared for electron backscatter diffraction (EBSD) by ion milling in a Fischione Instruments Model 1060 SEM Mill. Orientation maps of a region encompassing the melt pool of each sample were acquired by utilizing FEI Apreo and Scios scanning electron microscopes (SEMs), each equipped with an EDAX EBSD detector, at 20 kV, spot size 13, and step size of 2.5 µm (0.5 µm for limited areas). OIM Analysis software generated maps from EBSD data. For each map, data points not meeting confidence index (CI) and/or image quality (IQ) thresholds were assigned to black (as seen in the Results). In some cases, a second map was acquired with identical settings immediately following the first, in order to test if single, highly misoriented points with moderate or high CI/IQ would remain. A new set of such data points appeared in new positions on the second map, thus generally confirming the spurious nature of the orientation information at those points. Neighbor correlation, which would set points with low CI and/or IQ to a neighbor's orientation and is a common post-processing step for EBSD maps, was not performed so as to keep the positions of such points visible to the reader.

Near-field high-energy diffraction microscopy (HEDM) experiments [37–41] were performed at beamline ID1A3 of the Cornell High Energy Synchrotron Source. These x-ray measurements generate reconstructions of three-dimensional spatial lattice orientation fields in probed diffraction volumes. Data was collected from three transversely sectioned samples (consisting of one half of the laser track and surrounding material (see Fig. 1). For each sample, processing of near-field data produced a spatial grid (grain reconstruction) with 20 µm resolution which describes how each point in the grid is oriented relative to a sample reference frame. This data is similar to that produced using EBSD, but in three-dimensions and at lower spatial resolution. The reconstruction limited candidate orientations to those that fall within a misorientation band of ±3° from the primary single crystal orientation, determined from a complementary far-field HEDM measurement that was sensitive to the distribution of orientation present (but provided no spatial information). The bounds were applied to each of three values of the angle-axis orientation parametrization in 0.25° steps, producing 25^3 = 15,625 candidate orientations. We note that stray grains were not able to be reconstructed using HEDM due to the major difference in measured intensity between small stray grains and large primarily single crystal matrix in which they are embedded[1]. Associated confidence values of the orientation reconstruction at each spatial point were computed based on the presence of intensity at expected positions (completeness). From each reconstruction, misorientations were calculated relative to a reference orientation or relative to other points, as further detailed in the Results section. The experimental setup and data processing are described in more detail in the Supplementary material.

Finally, samples (half-tracks) were further sectioned along the laser travel direction (longitudinal cross-section), and sample preparation, optical microscopy and EBSD repeated as described previously.

[1] The far-field detector's dynamic range, coupled with selected parameters for data processing, did not provide means to detect crystallites on the order of tens of µm within a mm-size single-/oligo- crystal.

Table 1: Laser process parameters used and corresponding determination of presence of a re-solidifed melt pool.

Sample (*P* [W] - *V* [mm/s])	100-0.5	100-1	100-2.5	200-2.5	250-2.5	250-5	250-10
Melt pool identified	No	No	No	Yes	Yes	Yes	Yes

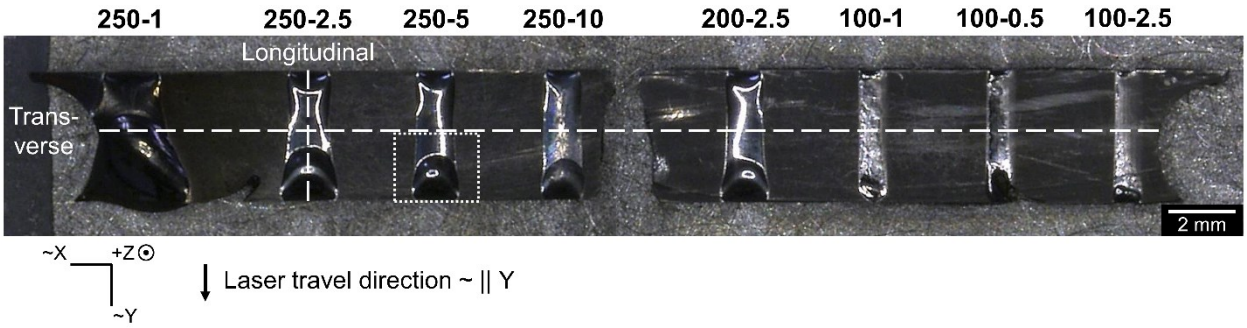

Fig. 1: Top view of substrates after re-solidification. P-V parameters are noted above each track. Dashed lines indicate orientation of sectioning planes; dotted line typifies the half-tracks used in HEDM experiments. Track at far left (250-1) is not reported due to excessive melting which deformed the substrate's outer dimensions.

Results

Solidification morphology

Optical micrographs (Fig. 2) show transverse cross-sections of each sample's melt pool after etching[2], revealing cellular and dendritic solidification structures with solidification directions that vary with location. While the solidification direction was out of plane in the central, lower depth (higher) region of each melt pool, the direction in a broad region about the melt pool's perimeter was more or less radial (pointing towards the top-center). Higher magnification micrographs show this predominantly radial directionality more clearly in the right column of Fig. 2. Brighter elliptical areas, marked by solid arrows in Fig. 2 and only seen on the *P* = 250 W, *V* = 10 mm/s section, were most likely grains (see EBSD results in next section).

Longitudinal cross-sections (Fig. 3(a)) provided an alternative view of the solidified structures, and are shown with higher magnification in Fig. 3(b).

In each sample except *P* = 250 W, *V* = 10 mm/s (hereafter referred to as 250-10), above the continuous etched line that marks the furthest extent of melting, the bottom of the solidified melt pool was formed by a featureless strip (marked "Planar" in Fig. 3(c)). Higher, after the appearance of initial perturbations with fine spacing, cellular growth proceeded with coarser spacing and generally upwards. After some length, cell boundaries rotated towards the direction of laser travel (magnified views of Fig. 3(d) show

[2] The authors recognize that the transverse cross-sections of the 250-2.5 and 250-5 samples have been over-etched. Due to longitudinal sectioning, the complete transverse surfaces are no longer available. Furthermore, the presence of cracks in some micrographs is noted. It is believed that some cracks were pre-existing, although they may have been augmented and/or additional cracks may have been created during preparation for microscopy, based on JT's experience.

that this transition was continuous, with no abrupt change in direction) except for 250-10. Finally, in the region nearest the top of all samples but 250-10, cell boundaries closely followed the laser travel direction (horizontal).

The 250-10 melt pool followed a different path to solidification than the others just described. After the vertical growth region – which contained the least continuous vertical boundaries of all samples, as well as the coarsest spacing between vertical boundaries – continuous rotation of the solidification direction did not occur. Instead, at the top ends of the vertical boundaries, the boundary spacing became finer and significant side-branching began, appearing on the section surface in directions ranging from horizontal to diagonal (45°). Diagonal boundaries then replaced vertical boundaries. Higher in the melt pool, horizontal boundaries competed with the diagonal boundaries. Finally, the discreetly different spacing and shape of solidification features in a horizontal band at the top of the section may have been evidence of a grain (later confirmed by EBSD – see description of results for 250-10 in next section). Regions marked in Fig. 3(c) correspond to the segments of solidification just described.

Cracks visible in the micrographs may or may not have been present prior to surface preparation.

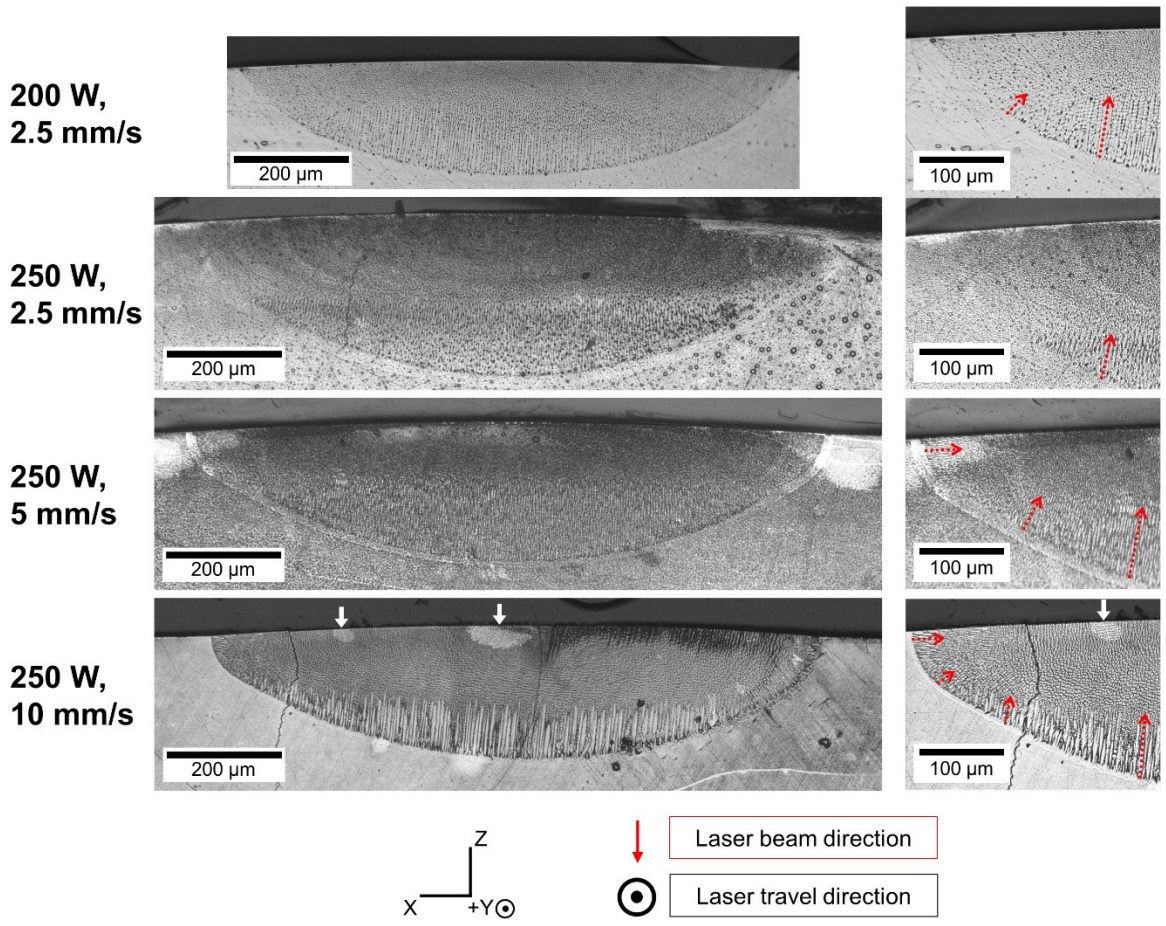

Fig. 2: Optical micrographs of transverse sections, including full views of re-solidified tracks (left column) and higher magnification views of left extreme of each track. Arrows overlaid on right column indicate local solidification direction.

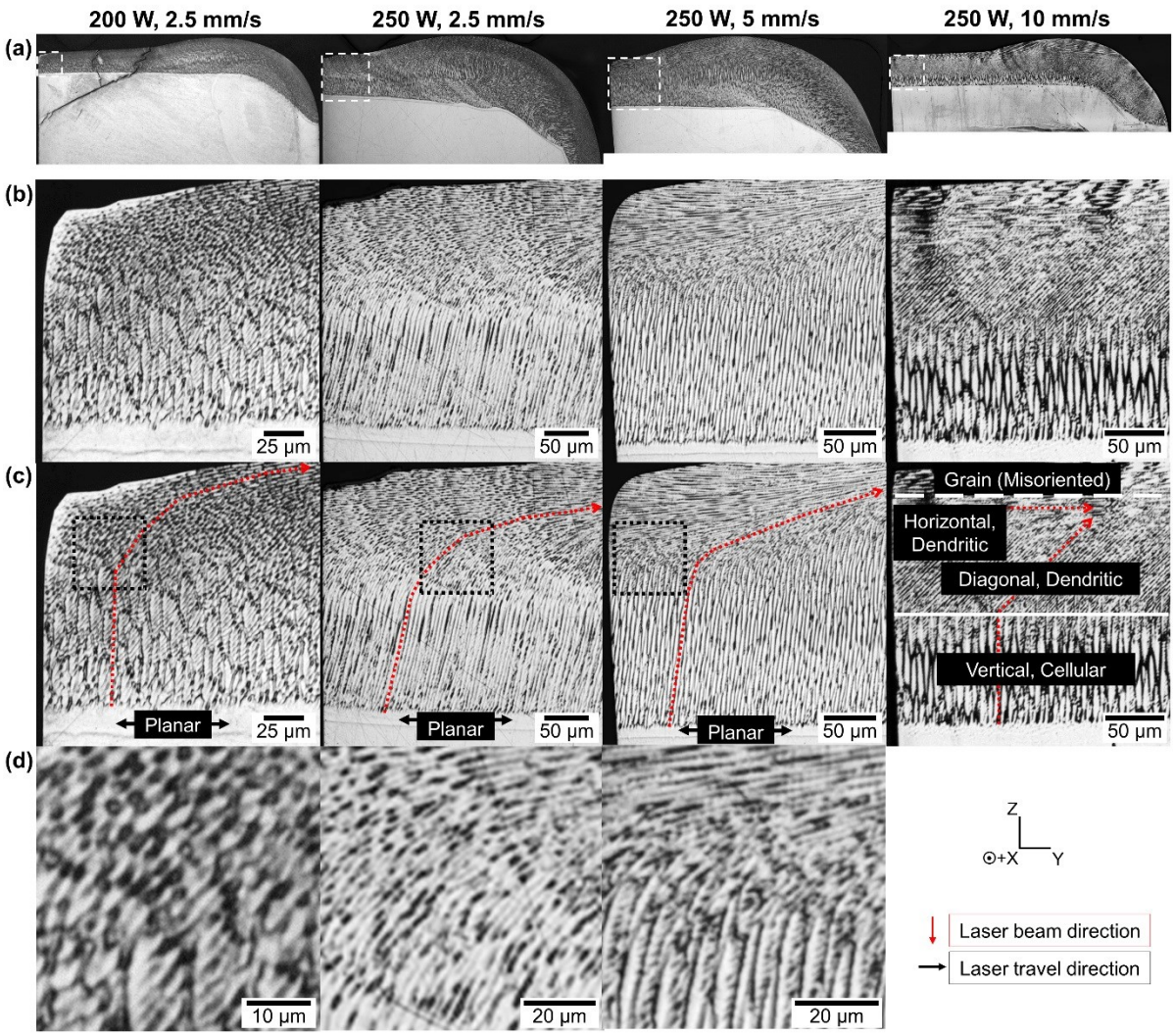

Fig. 3: Optical micrographs of longitudinal sections, including (a) entire sample, (b) higher magnification of areas marked by dashed squares in (a), (c) higher magnifications with overlaid solidification direction (red dotted line) and labeling of regions by solidification morphology, (d) magnified views of area marked by dotted squares in (c) demonstrating the continuous rotation of solidification direction in all sample except P = 250 W, V = 10 mm/s. The left edge of each sample was the transverse sectioning plane.

Crystallography and microstructure

EBSD maps

EBSD inverse pole figure maps, Fig. 4, were generated to show the crystallographic direction normal to the section surface. Maps of transverse sections of the 200-2.5, 250-2.5 and 250-5 samples contained only orientations with the [001] direction nominally aligned with the sample surface, and so the entirety of each surface appears to have an epitaxial relationship with the base crystal. For these three samples, the melt pool boundary could not be identified from the orientation maps, and its position was determined by comparison with image quality maps, secondary electron micrographs, and/or common features found on optical micrographs.

The fourth transverse EBSD map revealed grains in the 250-10 sample. Grains which grew near the bottom of the melt pool were columnar in shape, with lengths ranging from approximately 25 µm to 50 µm and widths of up to approximately 20 µm; grains located within the melt pool or at its top edge had roughly equiaxed shape and a wide range of sizes. Martensite was also present[3].

Orientation maps of longitudinal sections of the first three (epitaxial) samples revealed departures from epitaxy not found in transverse maps. Small grains of lenticular cross-section were found beneath the exit topography in the 200-2.5 and 250-2.5 samples, having major and minor dimensions circa 20 x 10 and 70 x 20 µm, respectively (for 250-2.5, the grain is seen in Supplementary Fig. 2, acquired before further polishing removed it from the section).

A much larger pair of grains was found at the top edge of the longitudinal section of 250-5, forming a misoriented layer at the top of the melt pool. The two apparent grains formed a continuous layer of 30 – 45 µm thickness at the top of the melt pool, with misorientations of ~10–18° (relative to an arbitrary point below the melt pool). A less apparent but similarly shaped grain was found at the top of the 250-2.5 (light color at top edge) and also exceeded 10° of misorientation.

Turning to the longitudinal map of the 250-10 sample, the majority of re-solidified material at the sectioned surface followed the orientation of the base crystal, but grains were detected near and at the bottom of the melt pool, and a continuous grain occupied the top of the re-solidified track. The top-layer grain is more misoriented and larger than the similar grain found in the 250-5 longitudinal map. Martensite probably also made up the diagonally grouped black points at the right. Additionally, the region of diagonally-oriented boundaries made visible by etched contrast in Fig. 3 is visible as diagonal bands of contrast in the inverse pole figure map.

[3] Although diagonal features that may be mistaken for cellular growth are seen in the right half of the melt pool (and in other places) on the etched micrograph of the transverse section, micrographs taken prior to etching demonstrated that these are volumes of martensite, because twinning of martensite caused surface relief on the polished section. This was later confirmed when these regions did not index as cubic phases during EBSD mapping (parallel bands of black points). The 250-10 track was located at one end of the substrate, which was in turn taken from near the end of a section of single crystal ingot. In ingots of Ni-Mn-Ga grown by the Bridgman method, it is common for the ingot to change phase along the solidification direction due to inherent macrosegregation.

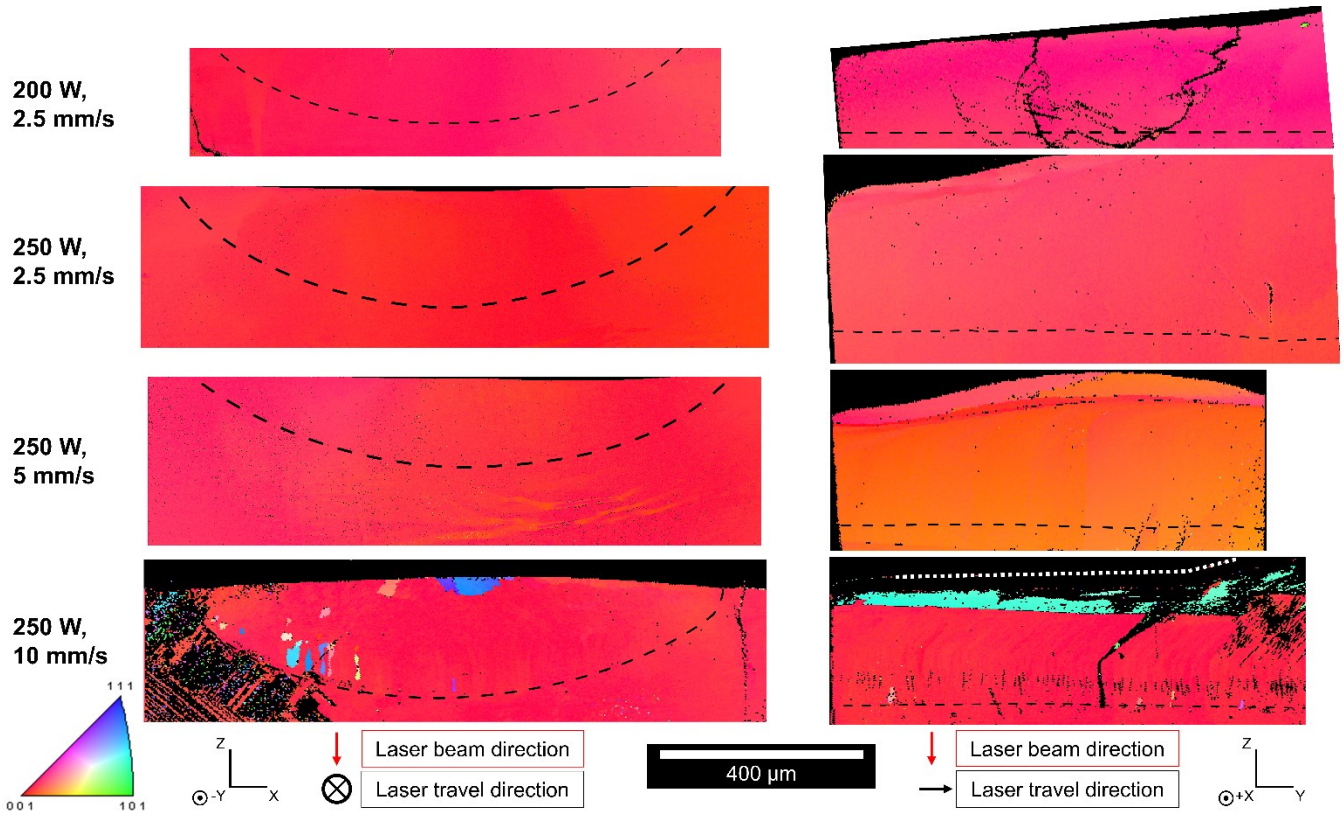

Fig. 4: Inverse pole figure maps generated from indexed EBSD scans, plotting the direction normal to the surface of the transverse (left column) and longitudinal sections (right column). Dashed lines indicate approximate melt pool boundary and dotted lines indicate sample edge (as needed). Note that topography of sample surface rises at top edge of longitudinal maps: Immediately at the left for 250-2.5 and 250-5, not until the right end for 200-2.5 and 250-10.

To verify that the cross-sections were free of grains of size near or below that of the scan step size, maps of step size 0.5 µm were collected within selected regions of the melt pools. An example of such a map (Supplementary Fig. 3) was typical of all areas which appear epitaxial in Fig. 4. The highest misorientation was about 2° relative to an arbitrarily selected orientation that was frequent in the higher-resolution map.

HEDM reconstructions

Fig. 5 presents orientation and misorientation data computed from each of the HEDM reconstructions. Although the HEDM experiment and data processing was not configured to detect small, misoriented grains due to technical reasons[1], orientation data is pertinent to epitaxial material. Misorientation maps in row (a) reveal that each HEDM sample contained small angle grain boundaries (SAGBs). Some of the SAGBs spanned across the melt pool boundary, based on estimates of each laser track's position within each reconstruction. Confidence maps (row (b)) show SAGBs as darker features in the same location as the misorientation maps, while also demonstrating relatively high confidence values throughout the reconstruction. Neither type of map displays any clear indication of the melt pool, except for an apparent "orientation drag" effect whereby like colors in row (a) are found further along the track centerline (in the direction of travel) compared to locations further from the centerline. To more closely examine if the melt pool can be visually recognized in the results, while also using a three-dimensional representation of crystal orientation, transverse sections were plotted in row (c) as inverse pole figure maps with a localized,

high-resolution color key generated using the MTEX package for MATLAB [42] and overlaid with the estimated location of the melt pool boundary. No distinct change of orientation across the melt pool boundary was seen.

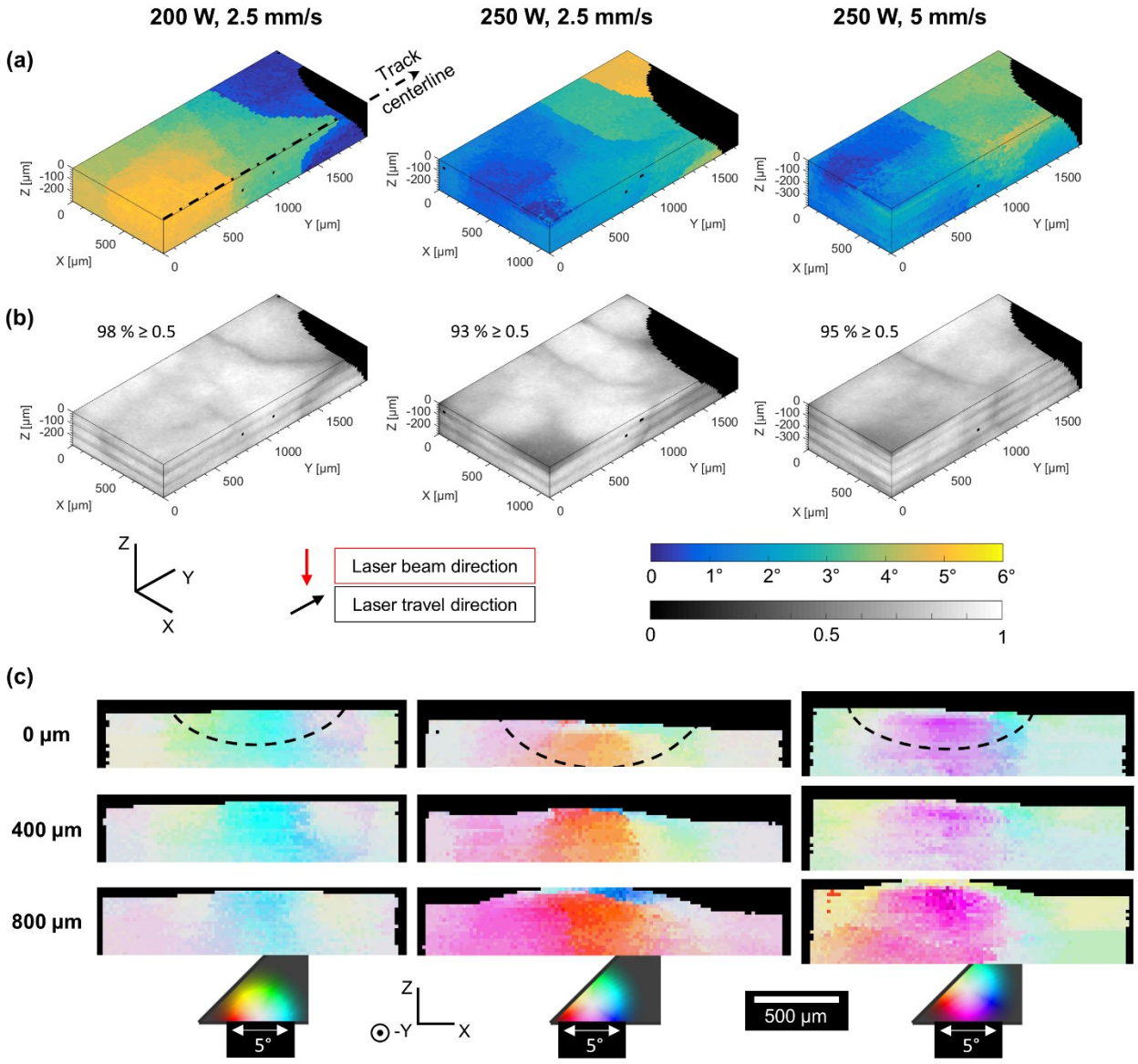

Fig. 5: Misorientation maps computed from HEDM reconstructions: (a) isometric view of horizontal, longitudinal and transverse sections (one half of reconstruction volume visible, corresponding to one half of area indicated by dotted line in Fig. 1). Top surface is located approximately at substrate surface (before melting); longitudinal surface is approximately coincident with track centerline; most common orientation within the bottom plane of each reconstruction used as reference. (b) Maps of confidence value corresponding to misorientation maps. Periodic low confidence along the Z direction is located at edges of scan layers; percentage of values over 0.5 is given for the entirety of each reconstruction. (c) Transverse sections (full width) colored by an inverse pole figure key spanning 5° (dashed lines indicate approximate melt pool boundary).

To allow more quantitative comparison of misorientation across re-solidified material and material not melted by the laser, misorientation was computed along sets of parallel lines constructed inside and outside of the melt pool. The bottom-most line in each set served as the reference, and so misorientation values are available for each higher line (top row of Fig. 6(a)); in this way, misorientation was examined from within the substrate to near-surface, along the direction normal to the surface. All lines had a width of five voxels, and so five orientations were averaged before computing misorientation. The first set was located along the laser track's approximate centerline, with the reference line directly below the melt pool[4], resulting in the bottom row of Fig. 6(a). Along each line, the misorientation of each point is given relative to the point located at the same longitudinal position on the reference line. Thus, the plots show the misorientation of material relative to the corresponding orientation below (or at[4]) the bottom of the melt pool, along the length of each laser track. Additional sets of lines were constructed to the left and right of the melt pool (schematic in Fig. 6(b)) in order to analyze non-re-solidified material in the same manner.

The values in Fig. 6(a) were low for the first two tracks (< 1°) but peaked when the line set crosses a SAGB. The values for the last track, 250-5, were higher and showed a stronger correlation with distance above reference.

Fig. 6(b) shows average misorientation values from an initial 400 µm segment of each line set. The reduced length avoided high values caused by intersection of the line set with a SAGB, and also reduced the likelihood that points beyond the quasi-steady state segment were used (we define this segment as the section of the track where surface topography and melting depth were largely constant with respect to position along the track). Average values for the 200-2.5 and 250-2.5 samples were near or below the 0.25° resolution of the reconstructions[5], but significantly above 0.25° to the left of and within the 250-5 track.

Additionally, to allow some comparison to mosaicity results found in literature (see discussion section), the misorientations between each point in the initial 400 µm of the reconstruction (Fig. 6(c)) were computed relative to all other points in that same volume. This resulted in the mean and maximum point-to-point misorientation values labeled "Both". The aforementioned volume was also divided into two, one containing no re-solidified material ("Outside"), and one containing the re-solidified track along with some non-re-solidified material below the track ("Track"). Mean and maximum values were higher for Track volumes than for Outside volumes in all three reconstructions. For each reconstruction, the mean for Track was approximately equal to that of Both, and maximum values were exactly equal to Both, indicating that the highest misorientations occurred between two points within the Track volume of each sample. Additionally, in the same manner, misorientations were computed between all points in the entire volume of each reconstruction. This final calculation gave means of 2.3°, 2.5°, and 2.5° and maximums of 6.3°, 6.5°, and 6.3° for the 200-2.5, 250-2.5, and 250-5 reconstructions, respectively.

[4] For 250-2.5, the scanned volume did not extend fully below the melt pool, but instead ended approximately at the melt pool's bottom. However, the volume included base crystal located at the sides of the laser track.

[5] The values may be below the 0.25° resolution due to the averaging of multiple orientations, which is described in the Supplementary material.

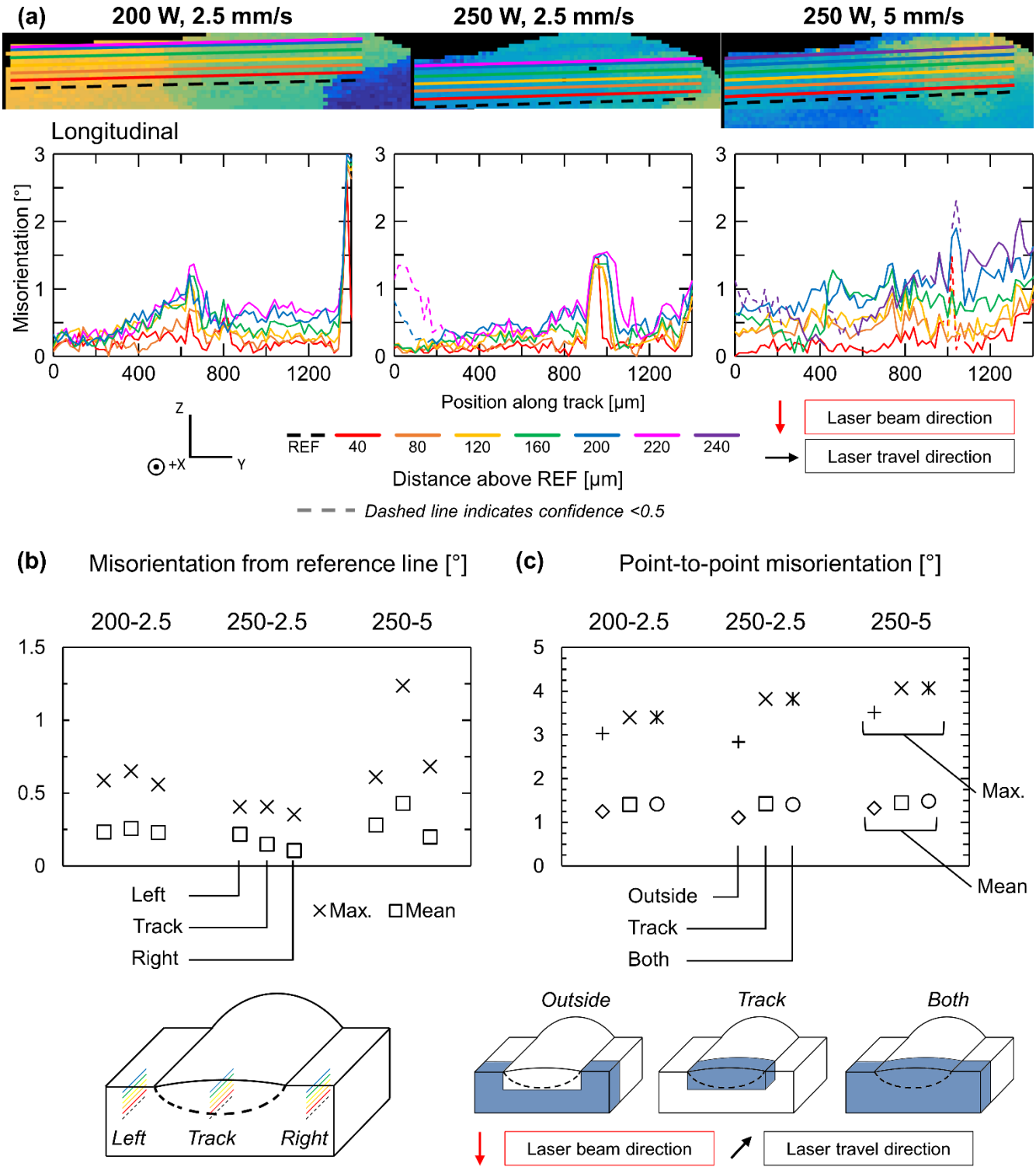

Fig. 6. Misorientation data computed from HEDM reconstructions. (a) longitudinal sections, and plots of misorientation relative to dashed reference line ("REF"), which is located approximately below bottom of melt pool (for 250-2.5, approximately at bottom of melt pool). (b) Misorientation for parallel line sets within track (reference below melt pool) and left and right of track (c) Misorientation between all points (voxels) in a selected sub-volume and all others in that sub-volume. Only points with confidence ≥ 0.5 used for (b) and (c).

Finally, Fig. 7 presents a plot of studied *P*-*V* pairs, classified by the general microstructure of the resultant sample.

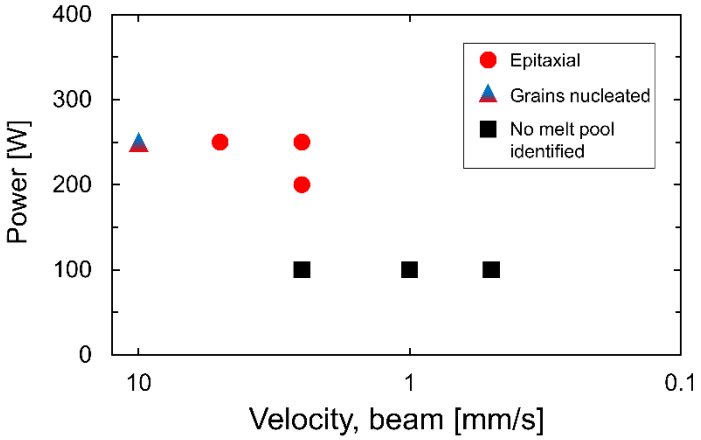

Fig. 7: Plot of track processing parameters and resulting microstructure. Determination of microstructures as epitaxial or as containing a significant proportion of grains was based on the quasi-steady state segments (QSS) of the tracks as presented in the preceding results, and determination of no melting in the remaining samples was made based on optical micrographs.

Discussion

Solidification morphology

The featureless strip found at the bottom of the melt pool on optical micrographs forms during planar growth [43] (however, such a region is difficult to see for the 250-10 sample due to near-absence of the continuous, etched line known as the fusion line or fusion boundary [44]). After some length, the planar interface transitioned to a cellular interface. However, the character of solidification present in all samples appeared more perturbed than the purely cellular mode in many places. Lancaster [45] and Lippold [44] referred to a mode intermediate to cellular growth and dendritic growth as “cellular dendritic growth”, and this term may apply to all samples except for the clearly dendritic growth found in sample 250-10. Regardless, for all melt pools but that of 250-10, the radial directionality of solidification directions seen in the transverse section and the change from vertical to parallel to the laser travel direction seen in longitudinal sections, shows that growth generally followed the local heat flow.

The discrete change in solidification direction from vertical to diagonal in sample 250-10 suggests that growth was dendritic at the location of this transition, because dendrites follow crystallographic directions rather than strictly adhering to the heat flow direction [46]. While we assume that the cubic phase B2’ solidifies along preferred growth directions of <100> under equiaxed growth conditions, epitaxy and a directional heat flow with moderate interface velocities dominated the situation in the present samples. At V = 10 mm/s, the solidification direction transitioned abruptly from <100> to a diagonal direction (perhaps <110>), which became favored as the heat flow vector rotated towards the horizontal. Thus, under the conditions studied and at P = 250 W, a beam travel velocity of V = 10 mm/s was high enough for a transition from cellular or cellular-dendritic to dendritic growth to take place at an intermediate depth. Further, the proportion of interruptions of cells (dendrites) by a neighboring cell (dendrite)

increased with increasing *V*, implying that competition between neighboring cells intensified as interface velocities increased.

Crystallography and microstructure

Presence of grains

Of the samples for which transverse EBSD maps show complete epitaxy (200-2.5, 250-2.5, 250-5), the grains detected in longitudinal sections represent a breakdown of epitaxy. Assuming that the size of these grains in all directions is on the same order, their detection depends on the chance of intersection with the section surface. Indeed, the removal of material by additional polishing was enough to remove a grain from the surface in one case (250-2.5).

However, the region covered by each longitudinal section, with the exception of 200-2.5 and 250-10, includes little of what we label as the "quasi-steady-state" (QSS) segment of the laser track, where the surface topography and depth of the melt pool is largely constant with respect to position along the track. As is made clear by the gradual increase in vertical position of the top edge of the track (tracing from the left-top corner), the majority or entirety of the section of track present during EBSD was beyond the QSS segment for samples 250-2.5 and 250-5 [6]. (The increase in vertical position of the top edge of each track can be seen more clearly in Fig. 3(a)). The top-layer grains detected in transverse cross-sections of 250-2.5 and 250-5 are thus located past the QSS segment. Furthermore, both small-size grains (on the order of 10 μm) noted earlier are also located past the QSS segment. It is plausible and necessary that thermo-fluid conditions in the melt pool change as it approaches the edge of the substrate, and the resultant buildup of thermal energy must lead to a decrease in thermal gradient at the solidification interface, along with the noted increase in melt pool depth. Such conditions may have become sufficiently favorable for nucleation in the presence of one or more nucleation sites.

The 250-10 track underwent a greater extent of nucleation as judged by the number and size of grains, and such nucleation and growth occurred clearly within the QSS segment. However, grains nucleated from the bottom of the melt pool were found almost exclusively on the left side of the melt pool, which borders pre-existing martensite in the single crystal. A possible explanation is that the substrate crystal contained more heterogeneous nucleation sites near the boundary between austenite and martensite (note that the horizontal direction of the transverse sections was parallel to the single crystal solidification direction of the single crystal used; and thus the boundary between phases is approximately vertical on the transverse sections).

Concerning the lack of grains in the HEDM reconstructions (meaning grains other than the large grains separated by SAGBs; small, highly misoriented grains or "stray" grains), we note that while small or highly misoriented grains would not be detected in misorientation maps (due to their exclusion from data processing), if such grains had some sufficient size, confidence values would be reduced in the volumes they occupy. Such a reduction in confidence would be akin to the visibility of SAGBs in the confidence maps (compare boundaries in row (a) to traces of low confidence in row (b) in Figure 5). Thus, it is plausible that the low confidence (< 0.5) regions at the top-center of the 250-2.5 and 250-5 tracks (front-top-right

[6] Material was lost during repeated preparation of the transverse sections of tracks 250-2.5 and 250-5, leaving a reduced length of track for longitudinal sectioning.

corner of each volume shown in row (b)) correspond to the top-layer grains detected by EBSD mapping of longitudinal sections (Fig. 4).

Effect of re-solidification on local crystallographic orientation

The shapes of melt pool boundaries were not identifiable in maps of crystal orientation, including those produced from HEDM reconstructions and EBSD scans (with the exception of track 250-10). This is consistent with epitaxial growth, with no change in crystal orientation taking place across the melt pool boundary. The only clear effect of the laser track on crystal orientation is the apparent "drag" of like color along the centerline in Fig. 5(a): near the ends of laser tracks 200-2.5 and 250-2.5, a SAGB appears to have been redirected along the direction of laser travel, thus extending the sub-grain which was on the incoming side of the boundary. While the data was collected after the pre-existing sub-grain structure was altered by re-solidification and so cannot directly confirm the "orientation drag" effect, it is implausible that the sudden change in the SAGB's shape about the laser line would have been produced during Bridgman single crystal growth. Furthermore, the shape is seen to be symmetrical about the track centerline when the half of the reconstruction not shown is made visible. Solidification directions approached the travel direction in the upper part of the melt pool, as seen on longitudinal optical micrographs (Fig. 3). Thus, in contrast with lower volumes that solidified by near-vertical growth, the upper fraction of each melt pool adopted crystal orientations from earlier positions of the laser spot, thus creating the "drag" shape.

Although the melt pool boundary was not clearly visible in the orientation maps, still, each high-angular-resolution inverse pole figure map (Fig. 5(c)) contains distinct regions of color which correlate roughly with the location of the center of the melt pool: blue for the 200-2.5 track, orange for 250-2.5 (turning to pink/purple at later cross-sections), and purple for 250-5. In the first two cases, these regions must be a result of either vertical growth from material below or from the "drag effect" which brought an orientation from an earlier (lower-Y) position of the laser spot (from an earlier cross-section). For 250-5, the purple region does not continuously run to the bottom of the map, and so it may have been introduced primarily by the "orientation drag". Separate from that effect, for each sample there are colors at the left and right sides of the melt pool which do not match the central region and extend from the sides of the melt pool boundary (refer to dashed line; e.g., seven through nine o'clock or five through three o'clock). The orientations from the sides were likely introduced to the melt pool due to the local solidification direction, which had a more-or-less radial distribution (inclined from the vertical in the direction of the centerline) along the perimeter of the melt pool as seen in Fig. 2.

Turning to the misorientation across parallel line sets, the average and maximum misorientation along the first 400 μm of the parallel lines constructed within track 250-5 (Fig. 6(b)) are significantly higher than for the other two tracks. The parallel lines in the non-melted-and-re-solidified material, to the sides of the tracks, serve as a control or comparison to the lines from the track itself. Of the outside sets, those surrounding the 250-5 track have the highest maximum misorientations, and the left set has the highest mean misorientation. Based on this measure, the material surrounding the 250-5 track had higher internal misorientation over a fixed distance than material surrounding the other two tracks. Therefore, it is likely that the 250-5 track encountered a greater spread of orientations for epitaxy during its passage through the base material. As a result, the spread of orientations within the melt pool may be higher than for the 200-2.5 and 250-2.5 tracks, within the segment studied. Additionally, it is plausible that "orientation drag" increased misorientation values for the parallel line sets (necessarily, this effect influences the orientation

in the track but leaves the reference line's orientations unchanged – if the reference line was correctly positioned beneath the melt pool).

Misorientation internal to a single grain or single crystal has been explained through the concept of mosaicity. Orientation can vary continuously, as demonstrated by EBSD measurements [47,48], and must be facilitated by crystal defects. A distribution of orientations has been measured by HEDM in annealed Ni grains and was wider than the reported resolution of that experiment [37]. For MSMAs, crystal mosaicity has been examined via reciprocal space mapping (RSM) of neutron diffraction [49] and laboratory-scale XRD [50]. Direct comparison with the cited works is not straightforward due to the differences between HEDM reconstruction and RSM (and also due to the relatively low penetration depth of laboratory-scale XRD); nevertheless, the reported mosaic spreads of 0.4 - 1° for XRD RSM [50] may be most comparable to the point-to-point misorientations in Fig. 6(c), which reach 2.8 – 3.5° outside of the tracks and 3.4 – 4.1° for volumes which contain the track. Likewise, the mosaic spread of 0.5° reported from neutron diffraction of a 3x5x7 mm sample [49], may be most comparable to the values for the whole reconstructions, which reach over 6°. Because mosaicity typically refers to the full-width half-maximum (FWHM) value of a peak-fit, the maximum point-to-point misorientation present in a given sample will be numerically higher than the sample's reported mosaicity. For that reason, if mosaic spread values for the present samples were available, they would be lower than the misorientation values given in Fig. 6(c) (for the same regions of the samples) and lower than the misorientation values of 6.3° – 6.5° computed for the entirety of each sample. Comparisons between the present samples and single crystals of various size and with various interaction volumes are not straightforward. Regardless, it has been suggested that low mosaicity (< 0.5°) is an indication of good MSMA crystal quality [49]. One study found that a crystal with a reported mosaicity of 1.7° had low twinning stress (< 2 MPa near the reverse martensitic transformation temperature), while crystals with lower mosaicities had both higher and lower twinning stresses [51]. Another study confirmed that SAGBs reduce fatigue life [52]. It is encouraging that, for the quasi-steady-state segments of the present samples, epitaxially re-solidified material had a spread in orientation which spanned at most 1° more of orientation space than did the spread for neighboring non-re-solidified material (2.8° vs. 3.8° for 250-2.5, Fig. 6(c)). Epitaxial material also was at most 1.2° misoriented from non-re-solidified material directly below (250-5, Fig. 6(b)).

Consequences of compositional variation

Since macrosegregation occurs during Bridgman growth of Ni-Mn-Ga (e.g. [36]), slight compositional variation may have been present in the substrate before the experiment, and might have affected the solidification behavior of one track in comparison to another. While we cannot presently exclude this possibility, we believe that small variations in composition [7] expected in the substrate (at points around/along the future location of a track, and also between the locations of tracks) would not have a significant effect on the growth of grains and would not alter the qualitative conclusions we drew about solidification modes. In any case, while microsegregation in Ni-Mn-Ga is undesirable for MSMA applications, the microsegregation seen in the tracks can be removed by a homogenization treatment as demonstrated for Ni-Mn-Ga and Ni-Co-Mn-Sn samples produced by direct laser deposition (LENS) in Refs. [34,53] (no microsegregation was visible on optical micrographs after heat treatment). Finally, evaporation may shift the overall composition of laser-processed material, and various laser energy

[7] We note that the apparent presence of martensite at one side of the 250-10 track can be caused by a compositional shift of just 2 - 3 at.-% [54] or less [55] from the nominal single crystal ingot composition.

densities might cause evaporation of unequal magnitudes. While compensating for evaporation by modifying the composition of the substrate would be a plausible approach to mitigating a shift, this is beyond the scope of the present article.

Effect of process parameters

Considering the effect of process parameters overall, three *P*-*V* pairs produced near-fully epitaxial tracks while a fourth did not, as outlined in the *P*-*V* plot (Fig. 7). The presence of misoriented grains within the fourth (250-10) track suggests that this higher velocity falls outside of the parameter space for epitaxy at *P* = 250 W (along with all other present process parameters, and given the unknown nuclei density [19], which is the density of heterogeneous nucleation sites that persisted after single crystal growth and remained dispersed throughout the substrate before laser melting). If track-to-track variation in substrate composition is negligible and if the possibility that the 250-10 track encountered a volume of substrate with more numerous nucleation sites or with pre-existing athermal nuclei are ignored, then the growth of grains can be attributed to the higher laser travel velocity and resultant higher interfacial velocities, which promote interface instability. As the grains cover a small fraction of the melt pool, it is possible that this parameter pair is located just outside of the envelope for full epitaxy and in the vicinity of the columnar-to-equiaxed transition. However, loss of full epitaxy with increasing *V* is opposite to the experimental results of Fujita et al. [33], who found that at fixed laser power, low travel velocities produced polycrystalline tracks while higher velocities produced single crystalline tracks. On the other hand, the present results may be consistent with the qualitative shape of the modelling-based *P*–*V* processing map of Gäumann et al. [19], which features a C-shaped curve: to the low-power side of the curve, melting results only in columnar (single crystalline) growth, while to the high-power side, only equiaxed (polycrystalline) growth occurs. Thus, if a fixed laser power results in a polycrystalline track, it will do so at an intermediate range of velocities. While both of the referenced works utilized CMSX-4, laser spot properties likely differ between the two, making comparison difficult because the spot energy distribution has a strong influence on the interfacial thermal gradients. (Disagreement between the two works was noted in [43]). Additional *P*-*V* pairs are needed to confirm the behavior of Ni-Mn-Ga using the present experimental setup.

No correlation was established between *P*-*V* parameters and internal misorientation or mosaicity of epitaxial, re-solidified material. Only one such connection is foreseeable, though not demonstrated here: a larger melt pool re-solidifies from a larger bounding surface with a consequently greater spread of orientations, depending on the quality of the base crystal.

Looking forward, our results provide direction for full-melting laser-based AM of MSMAs. First, a range of intermediate *P*-*V* parameters which produce epitaxy is available in the space between the demonstrated epitaxial parameters and the parameter set that produced grains (250 W, 10 mm/s). Under the laser spot diameter and other characteristics of our experiment, this range is roughly 200 – 250 W and 2 – 10 mm/s (however, higher laser powers were not attempted during this study). Second, at the end of the track, decreased heat transfer due to edge of the substrate leads to conditions which increase likelihood of grain nucleation and growth. While we kept the laser beam moving at constant speed over the edge, DED systems commonly decrease the travel velocity at a corner or end of a track, and this may also affect the likelihood of grain formation by decreasing interfacial thermal gradient. The preceding discussion is based purely on re-solidification of substrate material and neglects the effect of powder impingement upon the melt pool, which is necessary for DED, and the need to homogenize deposits to achieve desired MSMA

properties [34]. Nevertheless, single-crystalline microstructure was demonstrated in this work, as is necessary for the functionality of a dense MSMA part.

Conclusion

In summary, laser-melted tracks of $Ni_{51}Mn_{24.4}Ga_{24.6}$ single crystal solidified almost completely epitaxially for *P*-*V* combinations of 200-2.5, 250-2.5, and 250-5, but transitioned to partially equiaxed (polycrystalline) growth within the track created with parameters of 250-10. A very small grain was found within the epitaxial growth of the *P* = 250 W, *V* = 2.5 mm/s track and of the *P* = 250 W, *V* = 5 mm/s track; in both cases near the end of the track. During epitaxy, the mode of growth was cellular or cellular-dendritic and transitioned to dendritic in the *P* = 250 W, *V* = 10 mm/s track. HEDM reconstructions suggest that re-solidification did produce a mosaicity within the epitaxial material similar to that of the base crystal. At most, the spread in orientations was 1° higher in the track than in non-re-solidified material. The same results also show that the *P* = 250 W, *V* = 5 mm/s sample included the highest misorientation of epitaxial solid relative to non-re-solidified material directly below the melt pool; however, it is plausible that the higher misorientation in this sample can be attributed to pre-existing mosaic spread rather than to the *P*-*V* parameters. Our work shows that a Ni-Mn-Ga single crystal can solidify without detectable grains under thermal conditions produced by the heat source of a direct laser deposition system, within a readily accessible range of operating parameters. The results presented may serve as a starting point for development of a single-crystalline powder deposition process for magnetic shape memory alloys.

Acknowledgments

The authors sincerely thank K. Nygren for contribution to configuration of HEDM data processing tools and for instructing JT in their use, and acknowledge A. Acierno for his assistance before and during HEDM experiments and for carrying out DSC experiments, A. Mustafa for preparing the single crystal material, and T. Paplham for assistance with optical microscopy. JT thanks Prof. J. Wiezorek for helpful discussion. This work was partially supported by the National Science Foundation grant DMR-1808082, and was performed largely at the Materials Micro-Characterization Laboratory and in part at the Nanoscale Fabrication and Characterization Facility, both facilities of the University of Pittsburgh. PM acknowledges financial support through NSF DMR-1710640. This work is based upon research conducted at the Cornell High Energy Synchrotron Source (CHESS), which is supported by the National Science Foundation under awards DMR-1332208 and DMR-0936384.

References

[1] K. Schlüter, B. Holz, A. Raatz, Principle Design of Actuators Driven by Magnetic Shape Memory Alloys, Adv. Eng. Mater. 14 (2012) 682–686.

[2] P. Müllner, V.A. Chernenko, G. Kostorz, Large cyclic magnetic-field-induced deformation in orthorhombic (14M) Ni–Mn–Ga martensite, J. Appl. Phys. 95 (2004) 1531.

[3] A. Sozinov, N. Lanska, A. Soroka, W. Zou, 12% magnetic field-induced strain in Ni-Mn-Ga-based non-modulated martensite, Appl. Phys. Lett. 102 (2013) 021902.

[4] A. Saren, K. Ullakko, Dynamic twinning stress and viscous-like damping of twin boundary motion in magnetic shape memory alloy Ni-Mn-Ga, Scr. Mater. 139 (2017) 126–129.

[5] S.L. Taylor, R.N. Shah, D.C. Dunand, Ni-Mn-Ga micro-trusses via sintering of 3D-printed inks containing elemental powders, Acta Mater. 143 (2018) 20–29.

[6] M.P. Caputo, A.E. Berkowitz, A. Armstrong, P. Müllner, C.V. Solomon, 4D printing of net shape parts made from Ni-Mn-Ga magnetic shape-memory alloys, Addit. Manuf. 21 (2018) 579–588.

[7] W. Maziarz, P. Czaja, R. Chulist, A. Wójcik, Ł. Żrodowski, B. Morończyk, R. Wróblewski, M. Kowalczyk, Microstructure and magnetic properties of selected laser melted Ni-Mn-Ga and Ni-Mn-Ga-Fe powders derived from as melt-spun ribbons precursors, Metals (Basel). 11 (2021) 903.

[8] A. Mostafaei, K.A. Kimes, E.L. Stevens, J. Toman, Y.L. Krimer, K. Ullakko, M. Chmielus, Microstructural evolution and magnetic properties of binder jet additive manufactured Ni-Mn-Ga magnetic shape memory alloy foam, Acta Mater. 131 (2017) 482–490.

[9] M.P. Caputo, C. V. Solomon, A facile method for producing porous parts with complex geometries from ferromagnetic Ni-Mn-Ga shape memory alloys, Mater. Lett. 200 (2017) 87–89.

[10] V. Laitinen, A. Salminen, K. Ullakko, First investigation on processing parameters for laser powder bed fusion of Ni-Mn-Ga magnetic shape memory alloy, J. Laser Appl. 31 (2019) 022303.

[11] F. Nilsén, I.F. Ituarte, M. Salmi, J. Partanen, S.-P. Hannula, Effect of process parameters on non-modulated Ni-Mn-Ga alloy manufactured using powder bed fusion, Addit. Manuf. 28 (2019) 464–474.

[12] V. Laitinen, A. Sozinov, A. Saren, A. Salminen, K. Ullakko, Laser powder bed fusion of Ni-Mn-Ga magnetic shape memory alloy, Addit. Manuf. 30 (2019) 100891.

[13] V. Laitinen, A. Sozinov, A. Saren, M. Chmielus, K. Ullakko, Characterization of as-built and heat-treated Ni-Mn-Ga magnetic shape memory alloy manufactured via laser powder bed fusion, Addit. Manuf. 39 (2021) 101854.

[14] P. Lázpita, G. Rojo, J. Gutiérrez, J.M. Barandiaran, R.C. O'Handley, Correlation between magnetization and deformation in a NiMnGa shape memory alloy polycrystalline ribbon, Sens. Lett. 5 (2007) 65–68.

[15] P. Zheng, N.J. Kucza, Z. Wang, P. Müllner, D.C. Dunand, Effect of directional Solidification on Magnetic Field-Induced Strain in Ni-Mn-Ga Foams with Coarse Grains, Acta Mater. 86

(2015) 95–101.

[16] U. Gaitzsch, M. Pötschke, S. Roth, B. Rellinghaus, L. Schultz, A 1% magnetostrain in polycrystalline 5M Ni–Mn–Ga, Acta Mater. 57 (2009) 365–370.

[17] K. Ullakko, A. Sozinov, J. Järvinen, Is it possible to make single crystalline Ni-Mn-Ga devices by 3d printing?, in: ICFSMA'16 Fifth Int. Conf. Ferromagn. Shape Mem. Alloy., Sendai, Japan, 2016: p. 51.

[18] M. Gäumann, S. Henry, F. Cléton, J.-D. Wagnière, W. Kurz, Epitaxial laser metal forming: analysis of microstructure formation, Mater. Sci. Eng. A. 271 (1999) 232–241.

[19] M. Gäumann, C. Bezençon, P. Canalis, W. Kurz, Single-crystal laser deposition of superalloys: processing–microstructure maps, Acta Mater. 49 (2001) 1051–1062.

[20] J.W. Park, S.S. Babu, J.M. Vitek, E.A. Kenik, S.A. David, Stray grain formation in single crystal Ni-base superalloy welds, J. Appl. Phys. 94 (2003) 4203–4209.

[21] W. Liu, J.N. DuPont, Direct laser deposition of a single-crystal Ni3Al-based IC221W alloy, Metall. Mater. Trans. A. 36 (2005) 3397–3406.

[22] Y. Fujita, K. Saida, K. Nishimoto, Laser Epitaxial Cladding of Ni-base Single Crystal Superalloy, Mater. Sci. Forum. 580 (2008) 67–70.

[23] R. Vilar, A. Almeida, E. Costa, Structure of Ni-alloys deposited by laser powder deposition on single crystal superalloy substrates, ICALEO 2012 - 31st Int. Congr. Appl. Lasers Electro-Optics. (2012) 197–204.

[24] X. Do, D. Li, A. Zhang, B. He, H. Zhang, T. Doan, Investigation on multi-track multi-layer epitaxial growth of columnar crystal in direct laser forming, J. Laser Appl. 25 (2013) 012007.

[25] J. Xue, A. Zhang, Y. Li, D. Qian, J. Wan, B. Qi, N. Tamura, Z. Song, K. Chen, A synchrotron study of microstructure gradient in laser additively formed epitaxial Ni-based superalloy, Sci. Rep. 5 (2015) 14903.

[26] R. Acharya, R. Bansal, J.J. Gambone, S. Das, A Coupled Thermal, Fluid Flow, and Solidification Model for the Processing of Single-Crystal Alloy CMSX-4 Through Scanning Laser Epitaxy for Turbine Engine Hot-Section Component Repair (Part I), Metall. Mater. Trans. B. 45 (2014) 2247–2261.

[27] A. Basak, R. Acharya, S. Das, Additive Manufacturing of Single-Crystal Superalloy CMSX-4 Through Scanning Laser Epitaxy: Computational Modeling, Experimental Process Development, and Process Parameter Optimization, Metall. Mater. Trans. A. 47 (2016) 3845–3859.

[28] C. Körner, M. Ramsperger, C. Meid, D. Bürger, P. Wollgramm, M. Bartsch, G. Eggeler, Microstructure and Mechanical Properties of CMSX-4 Single Crystals Prepared by Additive Manufacturing, Metall. Mater. Trans. A. 49 (2018) 3781–3792.

[29] C. Bezençon, A. Schnell, W. Kurz, Epitaxial deposition of MCrAlY coatings on a Ni-base superalloy by laser cladding, Scr. Mater. 49 (2003) 705–709.

[30] R. Vilar, E.C. Santos, P.N. Ferreira, N. Franco, R.C. da Silva, Structure of NiCrAlY coatings deposited on single-crystal alloy turbine blade material by laser cladding, Acta Mater. 57 (2009) 5292–5302.

[31] M.E. Glicksman, Principles of Solidification, Springer, New York, 2011.

[32] S.L. Narasimhan, S.M. Copley, E.W. van Stryland, M. Bass, Solidification of a laser melted nickel-base superalloy, Metall. Trans. A. 10 (1979) 654–655.

[33] Y. Fujita, K. Saida, K. Nishimoto, Study of microstructure in surface-melted region of Ni-Base single crystal superalloy CMSX-4, Mater. Sci. Forum. 512 (2006) 313–318.

[34] J. Toman, P. Müllner, M. Chmielus, Properties of as-deposited and heat-treated Ni-Mn-Ga magnetic shape memory alloy processed by directed energy deposition, J. Alloys Compd. 752 (2018) 455–463.

[35] M. Rappaz, J.M. Vitek, S.A. David, L.A. Boatner, Microstructural formation in longitudinal bicrystal welds, Metall. Trans. A. 24 (1993) 1433–1446.

[36] D. Kellis, A. Smith, K. Ullakko, P. Müllner, Oriented single crystals of Ni–Mn–Ga with very low switching field, J. Cryst. Growth. 359 (2012) 64–68.

[37] C.M. Hefferan, S.F. Li, J. Lind, U. Lienert, A.D. Rollett, P. Wynblatt, R.M. Suter, Statistics of high purity nickel microstructure from high energy X-ray diffraction microscopy, Comput. Mater. Contin. 14 (2009) 209–219.

[38] U. Lienert, S.F. Li, C.M. Hefferan, J. Lind, R.M. Suter, J. V. Bernier, N.R. Barton, M.C. Brandes, M.J. Mills, M.P. Miller, B. Jakobsen, W. Pantleon, High-energy diffraction microscopy at the advanced photon source, JOM. 63 (2011) 70–77.

[39] D.C. Pagan, J. V. Bernier, D. Dale, J.Y.P. Ko, T.J. Turner, B. Blank, P.A. Shade, Measuring Ti-7Al slip system strengths at elevated temperature using high-energy X-ray diffraction, Scr. Mater. 142 (2018) 96–100.

[40] A.N. Bucsek, L. Casalena, D.C. Pagan, P.P. Paul, Y. Chumlyakov, M.J. Mills, A.P. Stebner, Three-dimensional in situ characterization of phase transformation induced austenite grain refinement in nickel-titanium, Scr. Mater. 162 (2019) 361–366.

[41] K.E. Nygren, D.C. Pagan, J. V. Bernier, M.P. Miller, An algorithm for resolving intragranular orientation fields using coupled far-field and near-field high energy X-ray diffraction microscopy, Mater. Charact. 165 (2020) 110366.

[42] F. Bachmann, R. Hielscher, H. Schaeben, Texture Analysis with MTEX – Free and Open Source Software Toolbox, Solid State Phenom. 160 (2010) 63–68.

[43] J.N. Dupont, Fundamentals of Weld Solidification, in: ASM Handbook, Vol. 6A Weld. Fundam. Process., ASM International, 2011: pp. 96–114.

[44] J.C. Lippold, Welding Metallurgy and Weldability, John Wiley & Sons, Inc., Hoboken, NJ, 2014.

[45] J.F. Lancaster, Metallurgy of Welding, 6th ed., Woodhead Publishing, 1999.

[46] W. Kurz, D.J. Fisher, Fundamentals of solidification, Trans Tech Publications, Switzerland, 1998.

[47] X. Gao, W. Zeng, Y. Wang, Y. Long, S. Zhang, Q. Wang, Evolution of equiaxed alpha phase during heat treatment in a near alpha titanium alloy, J. Alloys Compd. 725 (2017) 536–543.

[48] M. Pötschke, U. Gaitzsch, S. Roth, B. Rellinghaus, L. Schultz, Preparation of melt textured Ni-Mn-Ga, J. Magn. Magn. Mater. 316 (2007) 383–385.

[49] K. Rolfs, A. Mecklenburg, J.M. Guldbakke, R.C. Wimpory, A. Raatz, J. Hesselbach, R. Schneider, Crystal quality boosts responsiveness of magnetic shape memory single crystals, J. Magn. Magn. Mater. 321 (2009) 1063–1067.

[50] P. Cejpek, L. Straka, M. Veis, R. Colman, M. Dopita, V. Holý, O. Heczko, Rapid floating zone growth of Ni2MnGa single crystals exhibiting magnetic shape memory functionality, J. Alloys Compd. 775 (2019) 533–541.

[51] D. Musiienko, F. Nilsén, A. Armstrong, M. Rameš, R.H. Colman, P. Müllner, O. Heczko, L. Straka, Universality of Temperature Dependence of Twinning Stress in Ni-Mn-Ga 10M Martensite and Effect of Crystal Quality, SSRN Electron. J. (2020).

[52] T. Lawrence, P. Lindquist, K. Ullakko, P. Müllner, Fatigue life and fracture mechanics of unconstrained Ni-Mn-Ga single crystals in a rotating magnetic field, Mater. Sci. Eng. A. 654 (2016) 221–227.

[53] E. Stevens, K. Kimes, V. Chernenko, P. Lázpita, A. Wojcik, W. Maziarz, J. Toman, M. Chmielus, Effect of homogenization on the microstructure and magnetic properties of direct laser-deposited magnetocaloric Ni43Co7Mn39Sn11, J. Manuf. Sci. Eng. 142 (2020) 071006.

[54] N. Lanska, O. Söderberg, A. Sozinov, Y. Ge, K. Ullakko, V.K. Lindroos, Composition and temperature dependence of the crystal structure of Ni–Mn–Ga alloys, J. Appl. Phys. 95 (2004) 8074.

[55] M. Chmielus, Composition, Structure and Magneto- Mechanical Properties of Ni-Mn-Ga Magnetic Shape-Memory Alloys, 1st ed., Logos Verlag Berlin, Berlin, 2010.

[Add ISBN to Ref. 31 (Glicksman), 44 (Lippold), 45 (Lancaster), 46 (Kurz & Fisher), 55 (Chmielus) manually before submitting]